2D TM GPR Imaging Through a Multi-Scaling Multi-Frequency Approach in L^p Spaces

Marco Salucci, *Member, IEEE*, Claudio Estatico, Alessandro Fedeli, *Member, IEEE*, Giacomo Oliveri, *Senior Member, IEEE*, Matteo Pastorino, *Fellow, IEEE*, Sergio Povoli, Andrea Randazzo, *Senior Member, IEEE*, and Paolo Rocca, *Senior Member, IEEE*

Abstract—An iterative multi-scaling approach for solving the electromagnetic inverse scattering problem related to the imaging of shallow subsurface targets with the ground penetrating radar (GPR) is proposed. The approach combines the zooming properties of the multi-scaling technique with the reconstruction capabilities of an inexact-Newton method developed in L^p spaces. It is based on a multi-frequency processing that allows one to face the ill-posedness of the inverse scattering problem by exploiting the regularization properties of a truncated Landweber method. Experimental data, extracted from radargrams obtained by the GPR in a real situation, are used for validation. The reconstruction results are also compared with those from competitive alternatives such as a standard inexact-Newton method or a state-of-the-art multi-frequency CG-based approach.

Index Terms—Ground penetrating radar, Electromagnetic scattering inverse problems, Buried object detection, Banach spaces.

I. INTRODUCTION

AMONG the numerous applications of electromagnetic imaging, subsurface characterization has a relevant place. Indeed, the non-invasive recognition of buried regions plays a key importance for the discovery of historical remains in archaeology [1], the detection of buried utilities and landmines [2], search and rescue operations [3] as well as geophysical investigations [5]. In these applications, the standard measurement apparatus for the data acquisition is the Ground Penetrating Radar (GPR), which is nowadays available in many commercial implementations as well as tailored to specific uses and operating conditions [6], [7]. Notwithstanding, GPR data processing is still considered a challenging problem and different strategies have been proposed. They are devoted – in an increasing level of difficulty – to the qualitative detection of buried targets or the pointwise quantitative reconstruction of the dielectric properties of the scene under test [7]-[12]. Clearly, when a precise characterization of buried targets is needed – as several applications require – the second class of approaches is the best choice, but the quantitative retrieval of the properties of buried objects poses notable problems. The main one, which particularly emerges when strong scatterers are at hand, is the need of solving a nonlinear problem. This leads to the possible incurrence in local minima during the inversion process, which give rise to false solutions.

To mitigate such an issue, this paper is aimed at integrating the so-called iterative multi-scaling approach (IMSA) [13]-[15] with a nonlinear inverse scattering solution based on an inexact-Newton method (INM) [16], [17] by following a strategy already proposed in [11]–[13]. However, this latter was based on a standard Hilbert space technique and it has been widely demonstrated that the same approach developed in L^p spaces can provide better reconstructions, mainly in terms of reduction of the smoothing effects associated to Hilbert-space regularization techniques. Consequently, in this paper, the integration of an L^p-space inversion procedure within a multi-scaling scheme is evaluated for the first time, with the aim of assessing, both numerically and experimentally, its capabilities in enhancing the reconstruction of the dielectric proprieties from GPR data with respect to the bare INM and to previous versions of the IMSA. Moreover, the exploitation of data acquired at multiple frequencies can significantly increase both detection and characterization performance [18] in a context where the available information on the target is notably limited (e.g., GPR imaging). Therefore, it seems to be profitable applying a focusing technique, such as the IMSA, to enhance the reconstruction capabilities of the multi-frequency inversion developed in [19].

Essentially, the combined method proposed here is an iterative approach based on three nested loops: (a) an outer multi-scaling loop aimed at locating the regions-of-interest (RoIs) where the unknown scatterers are supposed to lie, (b) an intermediate loop that locally approximates the nonlinear

inverse problem with a sequence of Newton linearizations, and (c) an inner loop to yield a regularized solution by means of a truncated Landweber method. The key difference with respect to the approach in [11], [12] is the mathematical formulation of loops (b) and (c), which are developed in L^p spaces by following the guidelines presented in [17], [20], [21]. Such modifications/improvements allow one a full exploitation of the potentialities of the combined approaches to obtain more accurate reconstructions. It is worthwhile briefly recalling that the IMSA represents a suitable "countermeasure" against local minima problems that enables the use of local search strategies for solving the arising inverse scattering problems [14]. The improvements expected from such a combined inversion strategy are mainly evaluated by processing experimental data, although some numerical reconstructions are reported, as well.

The paper is organized as follows. Section II includes a brief description of the mathematical formulation of the proposed three-loops approach, while the outcomes from a numerical calibration phase are reported in Section III. The following two sections are concerned with the method assessment when processing synthetic (Sect. IV) and experimental (Sect. V) GPR data along with some comparisons. Some conclusions are finally drawn.

II. Mathematical Formulation

This section briefly reviews the mathematical formulation of the proposed approach. The problem geometry, which consists of a tomographic configuration in a two-layer environment, is sketched in Fig. 1. Electromagnetic sources and probes belong to the measurement domain Ω, which is located in the upper layer, whereas the investigation domain D_{inv} is an underground region with square cross section.
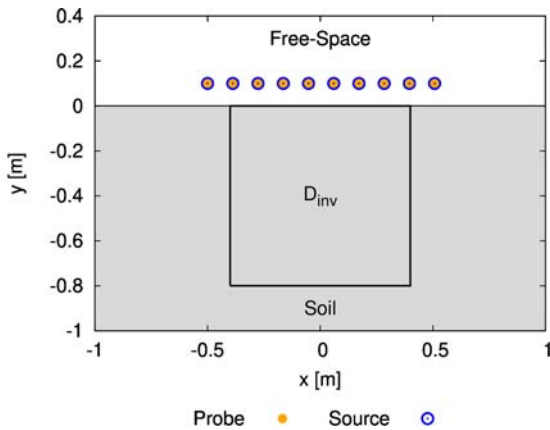
Fig. 1. Problem geometry. Investigation (D_{inv}) and measurement domains (Ω).

A. Inverse scattering problem

With reference to Fig. 1, a set of transverse-magnetic (TM) electromagnetic fields (generated by transmitting antennas) is used to illuminate the interface between the two half spaces, the lower and the upper ones being the soil and the air, respectively. Part of the incident wave is transmitted into the soil. The transmitting antennas are z-directed line-current

sources and they are excited by time-domain pulses $I(t)$, as widely done in GPR systems [7]. A set of frequency-domain data at frequencies $\{f_h; \ h = 1, \ldots, H\}$ is extracted from the signals received by the electromagnetic probes in Ω by means of the Fourier transform and processed to retrieve the dielectric properties of the underground region D_{inv}.

In order to work with frequency-independent unknowns, starting from the complex dielectric permittivity $\epsilon(\mathbf{r}) = \epsilon_0 \epsilon_r(\mathbf{r}) - j\sigma(\mathbf{r})/2\pi f$, where $\mathbf{r}$ denotes the position vector in the xy plane and ϵ_0 is the vacuum permittivity, the two following functions are defined:

$$x_\epsilon(\mathbf{r}) = \frac{\epsilon_r(\mathbf{r}) - \epsilon_{rb}}{c_\epsilon}, \qquad x_\sigma(\mathbf{r}) = \frac{\sigma(\mathbf{r}) - \sigma_b}{c_\sigma} \qquad (1)$$

where c_ϵ and c_σ are normalization coefficients for the relative dielectric permittivity $\epsilon_r(\mathbf{r})$ and the electric conductivity $\sigma(\mathbf{r})$, respectively, while the subscript "b" refers to the dielectric properties of the background. The position-dependent function x_ϵ and x_σ in (1) are then coded in a vector function $\mathbf{x}(\mathbf{r}) = [x_\epsilon(\mathbf{r}), x_\sigma(\mathbf{r})]^t$ so that the scalar TM inverse problem can be mathematically formulated throughout the following two equations, the multi-view extension being straightforward,

$$E_s^f(\mathbf{r}) = G_\Omega^f \left(\mathbf{T}(f) \cdot \mathbf{x}(\mathbf{r}) E_t^f(\mathbf{r}) \right), \mathbf{r} \in \Omega \qquad (2)$$

$$E_t^f(\mathbf{r}) = E_i^f(\mathbf{r}) + G_{D_{inv}}^f \left(\mathbf{T}(f) \cdot \mathbf{x}(\mathbf{r}) E_t^f(\mathbf{r}) \right), \mathbf{r} \in D_{inv} \qquad (3)$$

where E_t^f, E_i^f and E_s^f are the z-components of the total, incident, and scattered field, respectively. In these equations, $\mathbf{T}(f) = [c_\epsilon \quad c_\sigma/j2\pi f\epsilon_0]^T$ (the superscript T denotes the transposition operator), $\mathbf{T}(f) \cdot \mathbf{x}(\mathbf{r}) = \tau(\mathbf{r}, f)$ being the so-called *contrast function* at the frequency f, while G_Ω^f and $G_{D_{inv}}^f$ are the two well-known integral operators whose kernel is the half-space Green's function at f [22]. Following a widely adopted approach, the equations (2) and (3) are merged to yield a single functional equation for each frequency

$$E_s^f(\mathbf{r}) = \mathcal{L}_f(\mathbf{x})(\mathbf{r}), \qquad (4)$$

where the operator $\mathcal{L}_f$ is given by

$$\mathcal{L}_f(\mathbf{x})(\mathbf{r}) = G_\Omega^f [\mathbf{T}(f) \cdot \mathbf{x}(\mathbf{r})] \left[I - G_{D_{inv}}^f \left(\mathbf{T}(f) \cdot \mathbf{x}(\mathbf{r}) \right) \right]^{-1} E_i^f(\mathbf{r}). \qquad (5)$$

The data collected at all frequencies f_h, $h = 1, \ldots, H$, are combined in a set of nonlinear equations

$$\begin{bmatrix} E_s^{f_1}(\mathbf{r}) \\ E_s^{f_2}(\mathbf{r}) \\ \vdots \\ E_s^{f_H}(\mathbf{r}) \end{bmatrix} = \begin{bmatrix} \mathcal{L}_{f_1}(\mathbf{x})(\mathbf{r}) \\ \mathcal{L}_{f_2}(\mathbf{x})(\mathbf{r}) \\ \vdots \\ \mathcal{L}_{f_H}(\mathbf{x})(\mathbf{r}) \end{bmatrix}, \qquad (6)$$

then split into real and imaginary parts to define a real-valued problem of $2 \times F$ equations. This latter can be expressed in

compact form as follows

$$\mathbf{A}(\mathbf{x}) = \mathbf{b}, \qquad (7)$$

where $\mathbf{x} \in X$, $\mathbf{b} \in B$, and $\mathbf{A}: X \to B$, X and B being L^p Lebesgue spaces.

B. IMSA-MF-INLW Method - Overview

Equation (7) mathematically models a challenging inverse scattering problem, especially for the characterization of underground objects. The solution strategy outlined here addresses such an inversion problem according to three different guidelines. First, the whole procedure is enclosed in an iterative multi-scaling approach (IMSA) that keeps a suitable ratio between available data and unknowns to enforce a higher robustness against false solutions. Second, the frequency diversity is exploited by simultaneously processing the scattering data acquired at multiple frequencies (MF) as in (6). Third, the multi-frequency problem formulated at each step of by the multi-scaling procedure is solved by means of an inexact-Newton/Landweber (INLW) technique in L^p spaces to allow an accurate reconstruction of the dielectric properties of underground targets and their sharp discontinuities with a reduced impact of background artifacts and smoothing effects.

Such guidelines "translate" into three nested iterative loops. The outermost loop, which is based on the multi-scaling capabilities of the method, performs an adaptive iterative refinement/zooming of the RoI. The second and third loops implement the MF-INLW method. At each IMSA step, the equation (7) is sequentially linearized and solved by applying an L^p-space regularization procedure. This latter has been introduced for buried object detection in [23] and successively extended to multi-frequency imaging in [19], while, for the first time to the best of the authors' knowledge, it is combined here with the IMSA. A more detailed description of these implementations is presented in the following Section (Sect. II.C).

C. IMSA-MF-INLW Method - Three-Loop Structure

The structure of the inversion method is outlined in Fig. 2. To initialize the IMSA-MF-INLW method, a RoI that coincides with the whole investigation domain (i.e., $D_{(1)} = D_{inv}$) is considered first. Then, for each s − th ($s = 1,...,S$) IMSA step, equation (7) is solved in an investigation domain corresponding to the RoI $D_{(s)}$ by means of an MF-INLW algorithm developed in the framework of L^p spaces. The second (intermediate) loop generates a linearization of the operator $\mathbf{A}$, whereas the third (innermost) loop finds a regularized solution of the arising linearized problem. It is worth noting that, in the numerical implementation, each RoI $D_{(s)}$ is partitioned into a number of square cells, N, equal/close to the number of degrees of freedom of the scattered field [24]. It is worth noting that, since a mathematical treatment of the degrees of freedom in a nonlinear framework where unknowns/data are set in L^p spaces is not yet available, the value of N has been selected on the basis of the available L^2 analyses [25], [26]. However, it has been empirically found that, although approximate, this criterion allows obtaining

satisfactory results in the considered case studies, related to the inversion of both numerical and experimental data. Future developments will be also oriented toward the analysis of the degrees of freedom in the more involved L^p space framework.
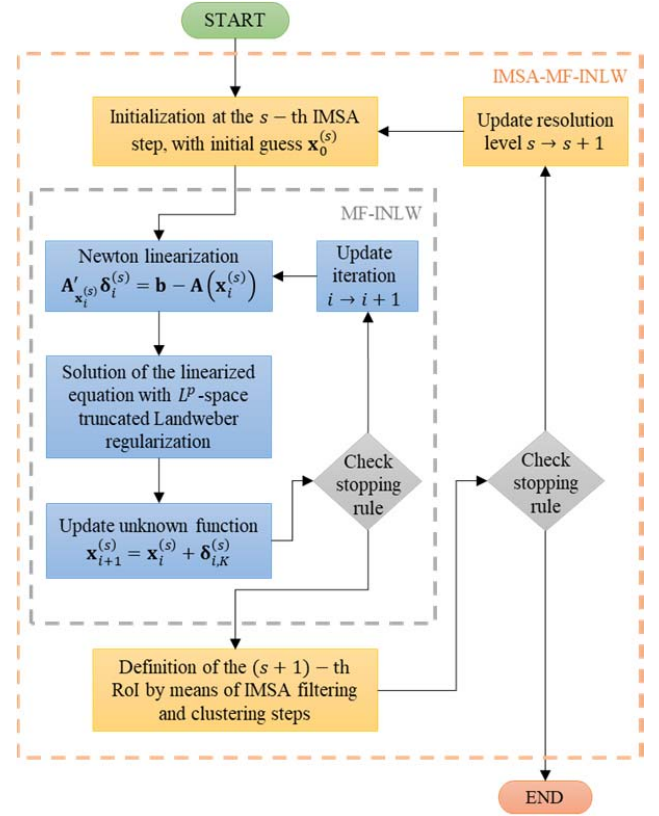
Fig. 2. Block diagram of the proposed IMSA-MF-INLW method.

For a more detailed description of the inexact-Newton approach (second and third loops), the interested reader can refer to [19], while hereinafter we just provide a quick outline of the method. The algorithm starts with an initial guess $\mathbf{x}_0^{(s)}$. Then, for each i-th ($i = 1,..., I$) iteration of the intermediate loop, the Newton linearization of the operator $\mathbf{A}$ is derived from its Fréchet derivative $\mathbf{A}'_{\mathbf{x}_i^{(s)}}$ around the reconstructed unknown $\mathbf{x}$ at the i −th linearization of the s −th IMSA step, $\mathbf{x}_i^{(s)}$. The yielded linear equation is solved in a regularized sense by recurring to a truncated Landweber regularization (innermost loop) in L^p spaces. This formulation requires significant modifications, which are based on the use of the so-called duality maps [17], to the corresponding one in the usually-adopted Hilbert space. The procedure starts with a null initial guess and the (innermost) Landweber steps are iterated K times ($k = 0,1,...K$). Once the innermost loop is terminated, the solution of the linearized equation (intermediate loop) is updated until a fixed number of iterations I has been performed or when a stopping criterion is fulfilled.

When the solution $\mathbf{x}_I^{(s)}$ has been found, a new ($s \to s+1$) IMSA step starts. More in detail, two processes are carried

out, namely the "filtering" and the "clustering" steps [14], which are aimed at locating the scatterer support by filtering out the background artifacts to define a new RoI $D_{(s+1)}$ possibly smaller than $D_{(s)}$. In such a way, a higher spatial resolution is adopted only within the RoI. The iterative zooming process is stopped at the s-th step ($s^{best} = s$) if one of the following conditions holds true:

1. The side of the zoomed investigation domain $D_{(s+1)}$ at the $(s+1)$-th step, $L_{(s+1)}$, is such that

$$\frac{|L_{(s+1)} - L_{(s)}|}{L_{(s)}} < \eta \qquad (8)$$

η ($0 < \eta < 1$) being a user-defined threshold;

2. The maximum number of IMSA (outer) steps has been reached (i.e., $s = S$).

III. CALIBRATION OF THE RECONSTRUCTION METHOD

Although the validation of the proposed approach has been carried out by processing experimental data for a more significant and reliable assessment of the achievable performance, the calibration parameters of the IMSA-MF-INLW have been derived from numerical test cases for which the ground-truth is always available. Towards this end, a simple scatterer like a cylinder with a square cross section (side: 0.08 [m]) has been assumed to be buried in the soil and centered at $(x_{obj}, y_{obj}) = (-0.08, -0.24)$ [m]. The upper half space has been assumed to be composed by air (similar to vacuum), while the lower half space has been characterized with $\epsilon_{rb} = 4.0$ and $\sigma_b = 10^{-3}$ [S/m]. The side of the investigation domain has been set to $L_{Dinv} = 0.8$ [m] and its barycenter has been located at $(x_{bar}^{Dinv}, y_{bar}^{Dinv}) = (0.0, -0.4)$ [m]. The scatterer has been chosen with dielectric properties equal to $\epsilon_{r,obj} = 5.5$ and $\sigma_{obj} = \sigma_b = 10^{-3}$ [S/m] so that $\tau = 1.5 + j0.0$. As for the multi-view/multi-illumination acquisition, the following parameters setup has been used: $V = 10$ (number of views), $x_{min}^{(v)} = -0.564$ [m], $x_{max}^{(v)} = 0.5$ [m], $y^{(v)} = 0.1$ [m] ($v = 1, \dots, V$) (positions of the sources); $M = 9$ (number of measurement points per-view), $x_{m,min}^{(v)} = -0.564$ [m], $x_{m,max}^{(v)} = 0.5$ [m], $y_m^{(v)} = 0.1$ [m] ($m = 1, \dots, M$; $v = 1, \dots, V$) (positions of the measurement points). The synthetic data for the inversion have been generated by solving the direct scattering problem with a time-domain electromagnetic solver based on the Finite-Difference Time-Domain (FDTD) algorithm (i.e., *GPRMax2D* [27], [28]). The square simulation domain has been assumed of side $L^{FDTD} = 6$ [m] and it has been partitioned into $N^{FDTD} = 750 \times 750 = 5.625 \times 10^5$ cells, the side of each cell being $l^{FDTD} = 0.008$ [m]. Moreover, the simulation time window has been set to $T^{FDTD} = 40 \times 10^{-9}$ [s], with a time step $\Delta t^{FDTD} = 1.89 \times 10^{-11}$ [s], so that the resulting number of time samples is $N_t^{FDTD} = 2120$. Perfectly matched layer (PML) boundary conditions have been adopted and the source type was an infinite current line excited by a Gaussian mono-cycle (i.e., first Gaussian pulse derivative, called "Ricker" in

GPRMax2D), with a central frequency $f_0 = 300$ [MHz], a 3-dB bandwidth between 200 and 600 [MHz] and a peak current amplitude equal to $I_{max} = 1.0$ [A]. Fig. 3 shows the pulse excitation waveform and the corresponding frequency spectrum. Moreover, the simulated data have been corrupted by a Gaussian noise characterized by a signal-to-noise ratio (SNR) on the time-domain total field equal to 40 [dB].

The quantities to be calibrated are the frequency steps (i.e., number of frequencies and the corresponding spacing Δf) and the following parameters of the reconstruction algorithm: I (the maximum number of intermediate iterations), K (the maximum number of innermost iterations), and p (the Lebesgue norm parameter). Moreover, the characteristic parameters of the IMSA have been chosen according to the outcomes of previous analyses [29], [30]: $N = 7 \times 7 = 49$ (number of discretization cells), $S = 6$ (maximum number of IMSA steps), and $\eta = 0.2$ (IMSA zooming threshold).
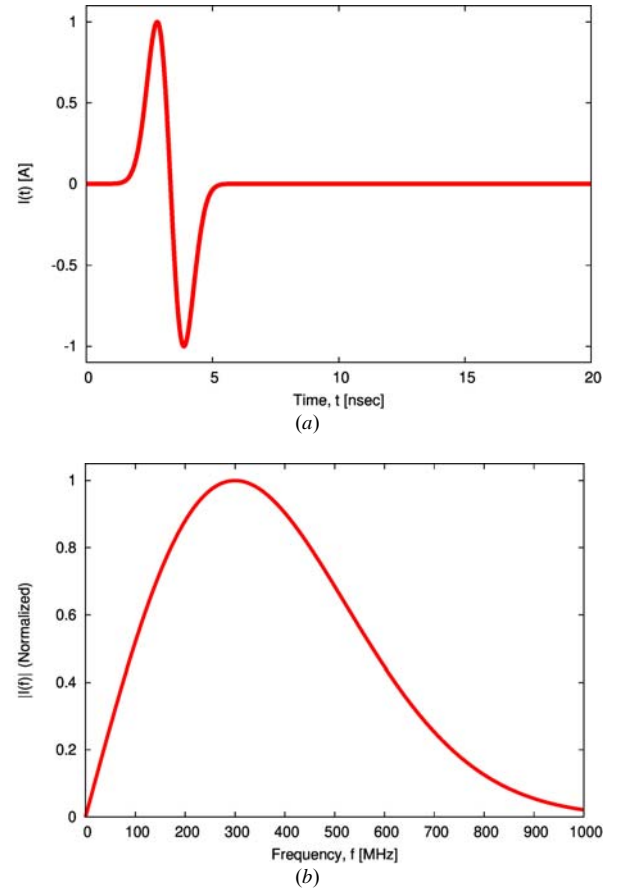
Fig. 3. *GPRMax2D* excitation signal: (*a*) time behavior and (*b*) normalized frequency spectrum.

The choice of the optimal values of the calibration parameters has been done by analyzing the following reconstruction indexes:

$$\Xi_{reg}(f) = \frac{1}{N_{reg}} \sum_{n=1}^{N_{reg}} \frac{[\tau(\mathbf{r}_n, f) - \hat{\tau}(\mathbf{r}_n, f)]}{[\tau(\mathbf{r}_n, f) + 1]}, \qquad (9)$$

where $\tau(\mathbf{r}_n, f)$ and $\hat{\tau}(\mathbf{r}_n, f)$ are the actual and the retrieved contrast functions at $\mathbf{r}_n$, while the subscript *"reg"* indicates whether the computation is related to the overall investigation domain ($reg \Rightarrow tot$), the actual scatterer support ($reg \Rightarrow int$), or the background region ($reg \Rightarrow ext$).
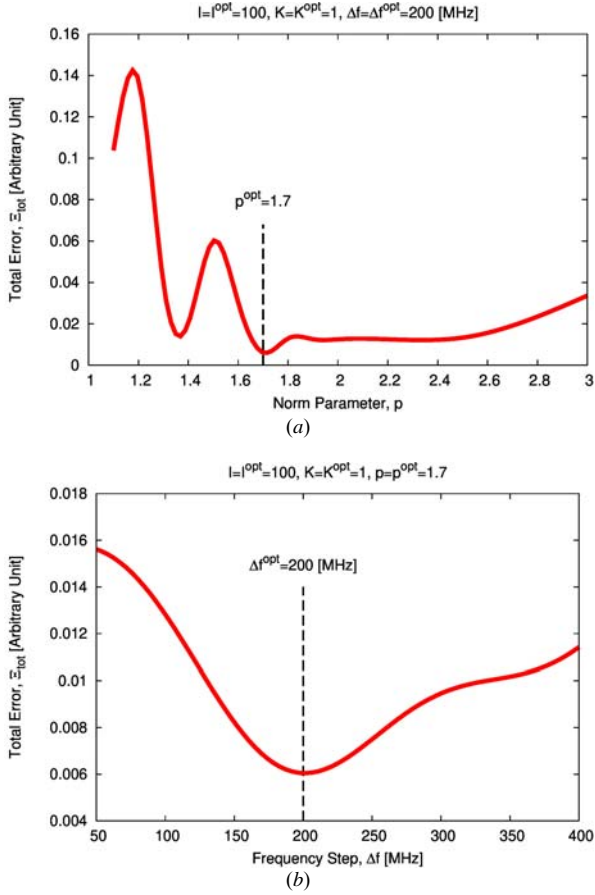
Fig. 4. *Calibration Phase* - Behavior of the total reconstruction error versus (*a*) the norm parameter p and (*b*) the frequency spacing Δf ($f = f_{min} = 200 \ [MHz]$).

An example of the results from this calibration phase is reported in Fig. 4 that refers to the case $f = f_{min} = 200 \ [MHz]$. Such a frequency has been selected since it is common to all reconstruction cases when changing Δf (the same happens for f_{max}, as well). The arising "optimal" (i.e., those corresponding to the minimum total error) values ($\Delta f^{opt} = 200 \ [MHz]$, $I^{opt} = 100$, $K^{opt} = 1$, $p^{opt} = 1.7$) have been kept in both the following numerical and experimental test cases.

To provide more insights on the zooming threshold in (8) and on its impact on the goodness of the results, the behavior of the total, internal, and external errors have been reported as a function of η in Fig. 5(*a*). It can be inferred that threshold values within the range $0.15 \le \eta \le 0.3$ yield optimal results, as quantitatively indicated by the lower value of Ξ_{tot}. Otherwise, a different choice of η determines a worsening of the reconstruction accuracy. More in detail, when η is too low (i.e., $\eta \le 0.1$), the zooming procedure tends to perform more

iterations than needed without adaptively stopping. As a matter of fact, once the RoI coincides with the actual support of the unknown target, the execution of one additional IMSA step (i.e., going from $s = 5$ to $s = 6$) leads to an undesired increase of the internal error [Fig. 5(*a*) and Fig. 5(*b*)]. On the other hand, when $\eta > 0.3$ the zooming procedure is prematurely terminated, and it stops immediately after the first low-resolution guess ($s = 1$) when $\eta \ge 0.4$. This causes an increase of the internal error due to an under-estimation of the contrast, and of the external error due to the presence of artifacts within the background region [Fig. 5(*a*) and Fig. 5(*b*)].
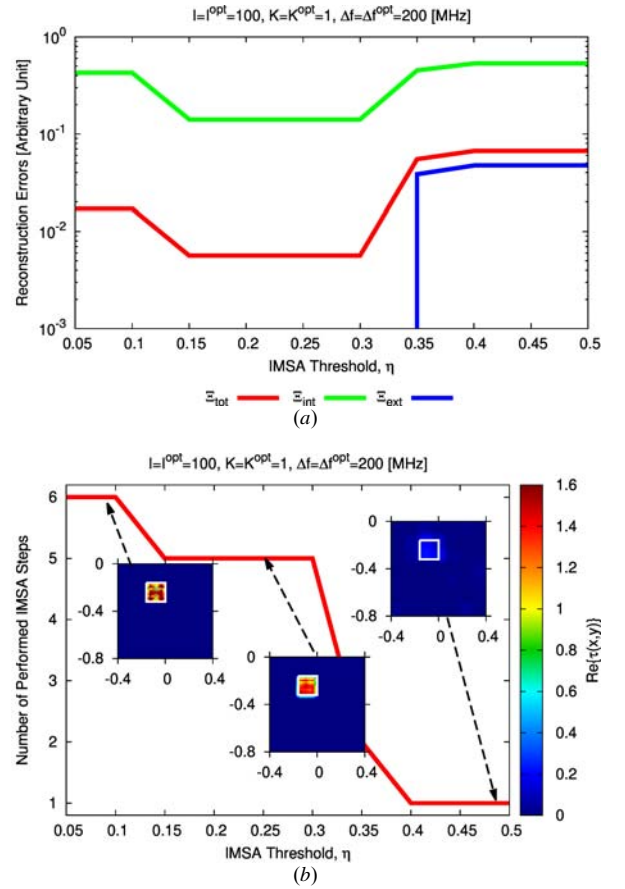
Fig. 5. *Calibration Phase* – (*a*) Behavior of the total, internal, and external reconstruction error and (*b*) number of performed *IMSA* steps with corresponding reconstructions versus the IMSA zooming threshold.

IV. NUMERICAL SIMULATIONS

While a large number of numerical simulations has been performed, but the main emphasis of this paper being on the experimental validation, just a synthetic example is discussed in this Section to explicitly confirm the IMSA-MF-INLW effectiveness when dealing with user-controlled data, as well. More in detail, such a representative example refers to the complex case of two separated buried bars. For this synthetic test case, the following assumptions have been made: 1) *top scatterer*: the barycenter is located at $(x_{bar}^{top}, y_{bar}^{top}) = (-0.08, -0.28) \ [m]$ and the size is $0.16 \times 0.08 \ [m^2]$; 2)

bottom scatterer: the barycenter is $(x_{bar}^{bottom}, y_{bar}^{bottom}) = (0.02, -0.48) \, [m]$ and the extension of the object support is $0.2 \times 0.08 \, [m^2]$. Both scatterers have a relative dielectric permittivity, $\epsilon_{r,obj}$, varying from 4.5 to 7.0 and $\sigma_{obj} = 10^{-3} \, [S/m]$, the properties of the background being the same of Sect. III. As for the measurement domain: $V = 10$, $x_{min}^{(v)} = -0.564 \, [m]$, $x_{max}^{(v)} = 0.5 \, [m]$, $y^{(v)} = 0.1 \, [m]$ ($v = 1, \ldots, V$); $M = 9$; $x_{m,min}^{(v)} = -0.564 \, [m]$, $x_{m,max}^{(v)} = 0.5 \, [m]$, $y_m^{(v)} = 0.1 \, [m]$ ($m = 1, \ldots, M; v = 1, \ldots, V$).

(a)

(b)
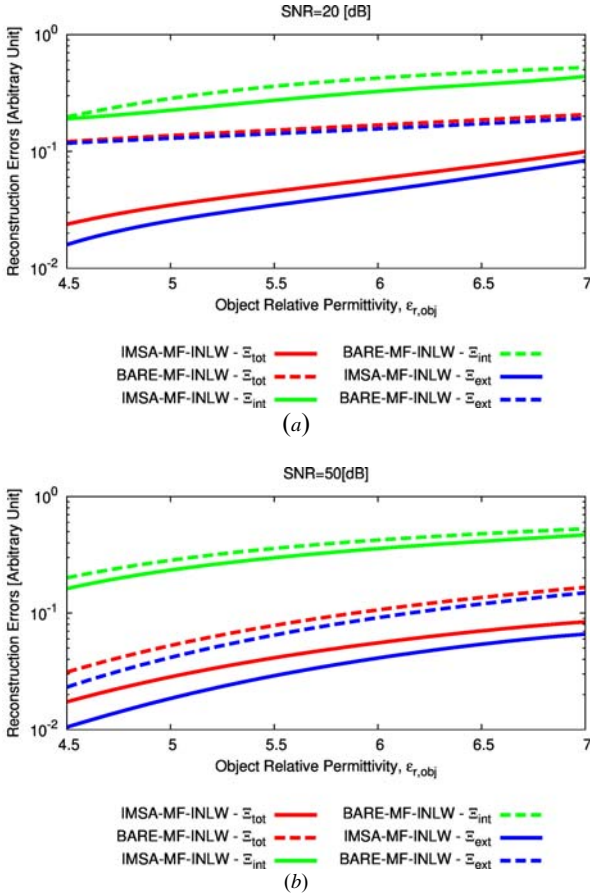
Fig. 6. *Numerical Simulations* [Two separated bars] - Reconstruction errors versus the dielectric permittivity of the targets. (a) $SNR = 20 \, [dB]$ and (b) $SNR = 50 \, [dB]$.

Fig. 6 plots the reconstruction errors (9) versus the dielectric permittivity of the scatterers when SNR = 20 [dB] [Fig. 6(a)] and SNR = 50 [dB] [Fig. 6(b)]. As expected, the values of the error indexes grow as the dielectric permittivity of the targets increases. For comparison purposes, the IMSA-MF-INLW performance are compared with those from a "bare" application of the INM (i.e., the innermost and the intermediate iterations) when setting the discretization of the investigation domain to $N = 20 \times 20 = 400$ square and choosing $I = 200$ (maximum number of external *IN* iterations), $K = 10$ (maximum number of internal LW iterations), and $p = 1.7$ according to [19]. In both noisy cases (Fig. 6), the "bare" method (dashed lines) gives reconstruction errors higher than the IMSA-MF-INLW approach. For

illustrative purposes, the final images of the reconstructed contrast function (real part) when $\epsilon_{r,obj} = 7.0$ are shown in Fig. 7. As it can be observed, the IMSA-enhanced approach turns out to be more reliable and efficient in locating and shaping the scatterers whatever the noise level blurring the scattering data.

Similar outcomes can be observed when varying the extension of the buried domain D_{inv}. As a matter of fact, considering the most challenging scenario (i.e., $\epsilon_{r,obj} = 7.0$ and $SNR = 20 \, [dB]$), the IMSA-MF-INLW is always able to correctly locate and shape the two unknown scatterers together with a good reconstruction of their contrast, as demonstrated by the reported results in Fig. 8(a) ($L_{Dinv} = 0.6 \, [m]$ - $\Xi_{int} = 3.56 \times 10^{-1} \, [m]$) and Fig. 8(b) ($L_{Dinv} = 1.6 \, [m]$ - $\Xi_{int} = 5.18 \times 10^{-1} \, [m]$). A remarkable robustness of the IMSA-MF-INLW is observed when changing the location of D_{inv} below the air-soil interface, as well. Indeed, the method is still capable of retrieving the two objects even when considering deeper domains, at the cost of a slight underestimation of their contrast because of the higher attenuation introduced by the lossy background [e.g., $y_{bar}^{Dinv} = -0.8$, $\Xi_{int} = 4.65 \times 10^{-1} \, [m]$ – Fig. 9(a); $y_{bar}^{Dinv} = -1.2$, $\Xi_{int} = 5.48 \times 10^{-1} \, [m]$ – Fig. 9(b)].

V. EXPERIMENTAL VALIDATION

In order to assess the proposed method in a real environment by completing the standard validations with synthetic data or laboratory-controlled measurements, the set of experimental data provided by the Near Surface Geophysical Group [31] has been adopted. In particular, the chosen benchmark is the NSGG Test Site 2 (TS2) - Sub Area 5 - Square B [32] and the input data come from the "DAT_0011" radargram file.

(a)   (b)

(c)   (d)
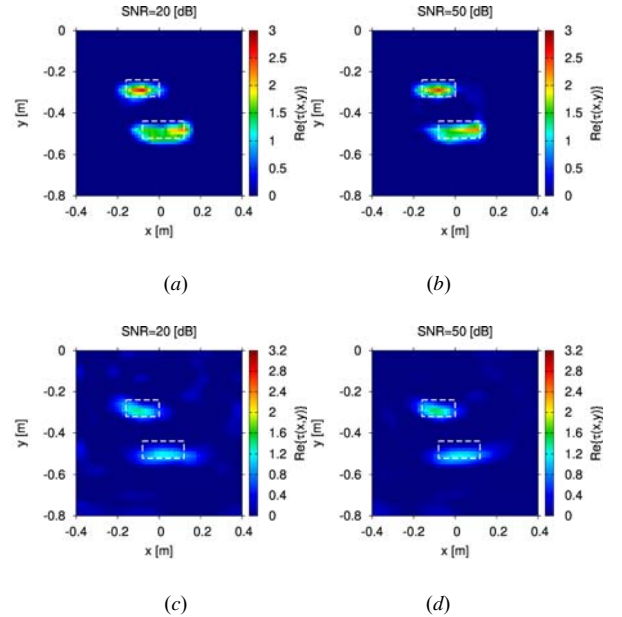
Fig. 7. *Numerical Simulations* [Two separated bars ($\epsilon_{r,obj} = 7.0$)] - Final image of the contrast function (real part) when (a)(c) $SNR = 20 \, [dB]$ and (b)(d) $SNR = 50 \, [dB]$ for the IMSA-MF-INLW (a)(b) and the "bare" MF-INLW (c)(d).

It refers to a homogeneous and nonmagnetic lower half space, whose estimated dielectric properties are $\epsilon_{rb} \cong 5.0$ and $\sigma_b \cong 38 \cdot 10^{-3}$ [S/m], where the investigation domain is a square region of side $L_{Dinv} = 0.8$ [m] centered at $(x_{bar}^{Dinv}, y_{bar}^{Dinv}) = (0.0, -0.45)$ [m], the distance between the air-soil interface and the top of D_{inv} being equal to 0.05 [m]. The buried scatterer, which lies in the investigation domain, is the sandstone rock shown in Fig. 10 whose dielectric properties – at $f = 100$ [MHz] – have been estimated in the ranges $2.0 \leq \epsilon_r \leq 5.0$ and $10^{-6} \leq \sigma \leq 10^{-5}$ [S/m] [9], [33]. The dimensions of the target are $0.35 \times 0.35 \times 0.20$ [m^3] and its depth is 0.33 [m].

(a)　　　　　　　　　*(b)*
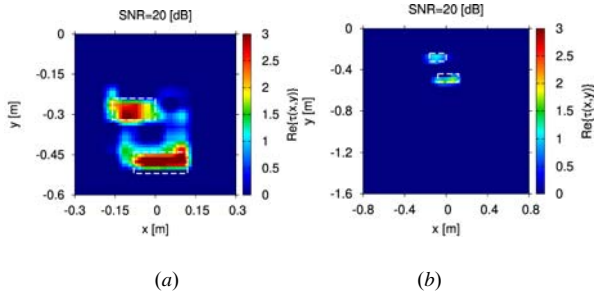
Fig. 8. *Numerical Simulations* [Two separated bars ($\epsilon_{r,obj} = 7.0$), $SNR = 20$ [dB]] - Final image of the IMSA-MF-INLW contrast function (real part) when considering a buried domain of side (*a*) $L_{Dinv} = 0.6$ [m] and (*b*) $L_{Dinv} = 1.6$ [m].

(a)　　　　　　　　　*(b)*
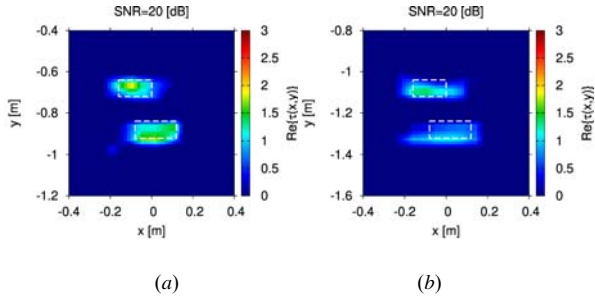
Fig. 9. *Numerical Simulations* [Two separated bars ($\epsilon_{r,obj} = 7.0$), $SNR = 20$ [dB]] - Final image of the IMSA-MF-INLW contrast function (real part) when considering a buried domain of side $L_{Dinv} = 0.8$ [m] located at (*a*) $x_{bar}^{Dinv}, y_{bar}^{Dinv}) = (0.0, -0.8)$ [m] and (*b*) $x_{bar}^{Dinv}, y_{bar}^{Dinv}) = (0.0, -1.2)$ [m].

Fig. 10. *Experimental Validation* - Sandstone rock. NSGG Test Site 2, Sub Area 5, Square B [31].

The measurement configuration is a bistatic one with a single TX antenna and a single RX antenna separated by $\Delta = 0.2$ [m]. The two antennas move along the observation line over the interface. The step between two consecutive traces in the radargram is 0.02 [m], while the number of views (i.e., the number of traces selected from raw radargram file) is $V = 5, 11, 21, 41$. The corresponding steps between the considered traces are 0.16 [m], 0.08 [m], 0.04 [m], 0.02 [m] (which represents the minimum available step). The positions of the measurement points belong to the range $\min\{x_m\} = \min\{x_v\} + \Delta$ and $\max\{x_m\} = \max\{x_v\} + \Delta$ along the x-direction, while $y_m = 0.0$ [m], $\forall m = 1, ..., M$ (i.e., ground coupled antennas). As an illustrative example, the measurement configuration with $V = 41$ is sketched in Fig. 11.
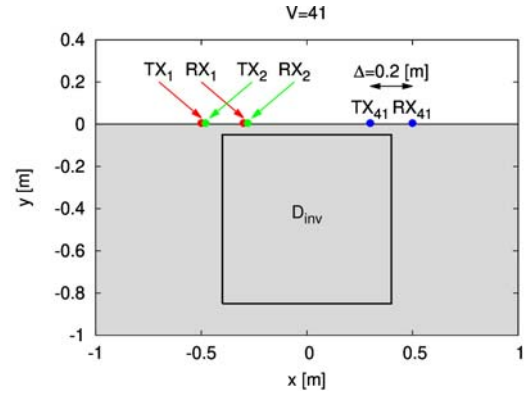
Fig. 11. *Experimental Validation* - Locations of TX and RX antennas above the soil interface ($V = 41$).

By setting the inversion parameters as in Sect. III, the IMSA-MF-INLW performance have been assessed comparatively with the "bare" application of the INM [19] and the IMSA-MF-CG approach [29], [30]. By keeping the same calibration setup of Sect. IV for the "bare" method, the following parameters have been chosen the IMSA-MF-CG method: $N = 7 \times 7 = 49$ (number of cells), $S = 6$ (maximum IMSA steps), $\eta = 0.2$ (zooming threshold), and $I = 200$ (maximum number of iterations). Due to the reduced bandwidth of the excitation signal in the experimental data (which is between 100 and 300 [MHz]), the frequency step has been reduced to $\Delta f = 100$ [MHz] in order to maintain the same number of processed frequencies found by the calibration ($H = 3$). The final reconstructions yielded by the three evaluated MF approaches are reported in Fig. 12 for different numbers of views, V. Both the real [Figs. 12(*a*)-12(*c*); Figs. 12(*g*)-12(*i*); Figs. 12(*m*)-12(*o*); Figs. 12(*s*)-12(*u*)] and the imaginary [Figs. 12(*d*)-12(*f*), Figs. 12(*j*)-12(*l*); Figs. 12(*p*)-12(*r*); Figs. 12(*v*)-12(*x*)] parts of the contrast function are provided. As it can be noticed, the IMSA-MF-INLW approach recovers satisfactory images of the scenario under test [Figs. 12(*a*)-12(*d*) (V = 5); Figs. 12(*g*)-12(*j*) (V = 11); Figs. 12(*m*)-12(*p*) (V = 21); Figs. 12(*s*)-12(*v*) (V = 41)], even though the reconstruction of the electric conductivity [Figs. 12(*d*), 12(*j*), 12(*p*), and 12(*v*)] is less accurate than that of the permittivity [Figs. 12(*a*), 12(*g*), 12(*m*), and 12(*s*)] because of the low contrast with respect to the propagation medium.
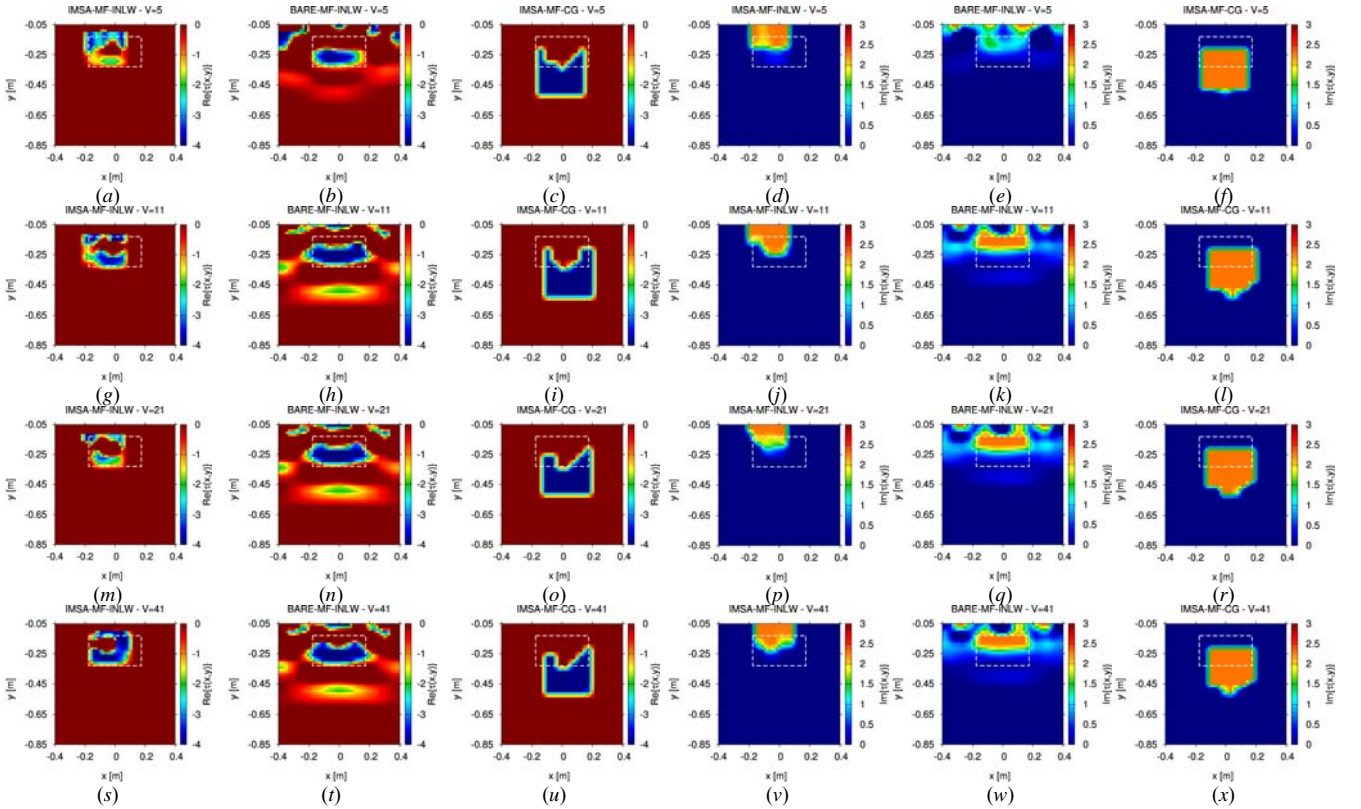
Fig. 12. *Experimental Validation* [$H = 3$ ($\Delta f = 100$ [MHz])] - Final reconstructions (real and imaginary parts of the contrast function). Comparison between the proposed approach, the "bare" solution and the IMSA-MF-CG method for different numbers of views (V).

On the other hand, it is worth pointing out that, as expected, the IMSA-enhanced approach always outperforms the "bare" solution [Fig. 12(*a*) vs. Fig. 12(*b*) and Fig. 12(*d*) vs. Fig. 12(*e*) (V = 5); Fig. 12(*g*) vs. Fig. 12(*h*) and Fig. 12(*j*) vs. Fig. 12(*k*) (V = 11); Fig. 12(*m*) vs. Fig. 12(*n*) and Fig. 12(*p*) vs. Fig. 12(*q*) (V = 21); Fig. 12(*s*) vs. Fig. 12 (*t*) and Fig. 12(*v*) vs. Fig. 12(*w*) (V = 41)].

To provide a more detailed and quantitative evaluation of the obtained results, the computed integral errors have been reported in Tab. I by assuming that the actual solution consists in a rectangle of size 0.35×0.20 [m^2] of depth 0.33 [m], permittivity $\epsilon_r = 3.5$, and $\sigma = 5 \times 10^{-6}$ [S/m]. As it can be observed, the IMSA-MF-INLW always yields remarkably lower values of Ξ_{tot} with respect to the BARE-MF-INLW.

TABLE I.
RECONSTRUCTION ERRORS FOR THE DIFFERENT TECHNIQUES VERSUS THE NUMBER OF VIEWS V. $H = 3$ ($\Delta f = 100$ [MHz]).

$\Xi_{tot} \times 10^{-1}$	$V = 5$	$V = 11$	$V = 21$	$V = 41$
IMSA-MF-INLW	5.55	7.77	6.93	7.43
BARE-MF-INLW	14.0	14.3	14.6	14.7
IMSA-MF-CG	6.69	8.22	7.52	7.50

Concerning the computational cost, the values of the CPU-time in Tab. II prove that the proposed multi-resolution method is significantly faster than its single-resolution counterpart.

TABLE II.
COMPUTATIONAL TIMES FOR THE DIFFERENT TECHNIQUES VERSUS THE NUMBER OF VIEWS V. $H = 3$ ($\Delta f = 100$ [MHz]).

Δt [sec]	$V = 5$	$V = 11$	$V = 21$	$V = 41$
IMSA-MF-INLW	48	59	66	78
BARE-MF-INLW	121	432	550	631
IMSA-MF-CG	99	138	267	462

Moving to the comparison between the IMSA-MF-INLW method and the IMSA-MF-CG technique [Figs. 12(*a*) and 12(*d*) vs. Figs. 12(*c*) and 12(*f*) (V = 5); Figs. 12(*g*) and 12(*j*) vs. Figs. 12(*i*) and 12(*l*) (V = 11); Figs. 12(*m*) and 12(*p*) vs. Figs. 12(*o*) and 12(*r*) (V = 21); Figs. 12(*s*) and 12(*v*) vs. Figs. 12(*u*) and 12(*x*) (V = 41)], it turns out that the former tends to slightly underestimate the size of the target (especially when the number of views V is low), whereas the latter overestimates it. Moreover, the IMSA-MF-CG prediction of the depth of the rock under the surface gets worse, while it better performs in estimating the electric conductivity [Fig. 12(*f*) vs. Fig. 12(*d*) (V = 5); Fig. 12(*l*) vs. Fig. 12(*j*) (V = 11); Fig. 12(*r*) vs. Fig. 12(*p*) (V = 21); Fig. 12(*x*) vs. Fig. 12(*v*) (V = 41)] even though the target dimensions are once again overestimated and the distance from the interface is not properly detected.
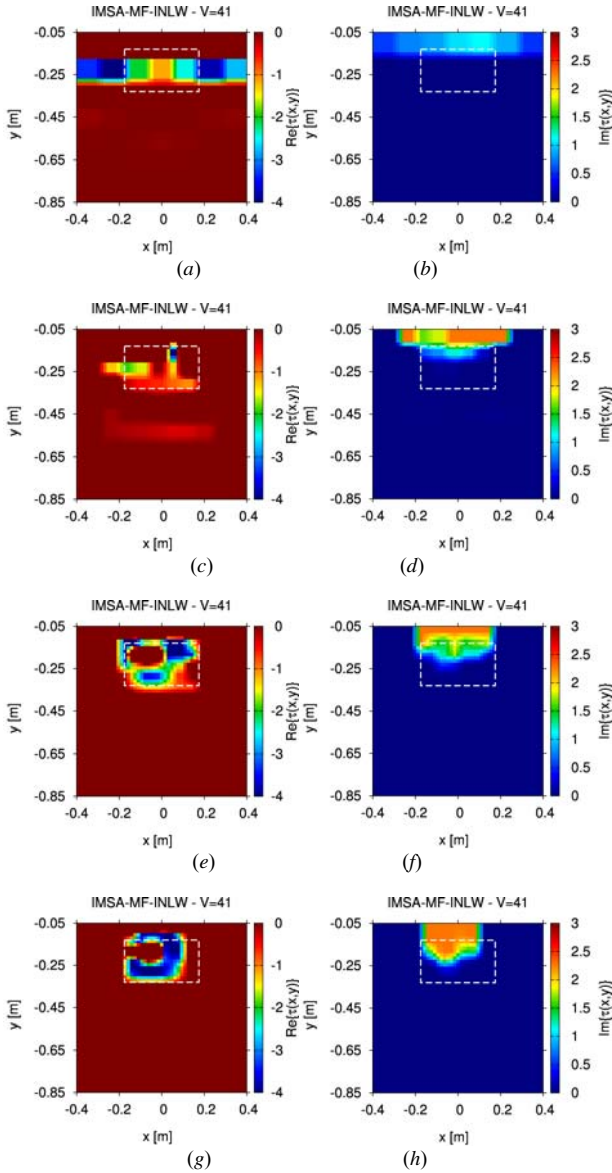
Fig. 13. *Experimental Validation* - Reconstruction obtained by the proposed approach for different steps of the IMSA external iterations for $V = 41$, $H = 3$ ($\Delta f = 100$ [MHz]). (*a*) Real and (*b*) imaginary parts of the contrast function at IMSA steps (*a*)(*b*) $s = 1$, (*c*)(*d*) $s = 2$, (*e*)(*f*) $s = 3$, and (*g*)(*h*) $s = 4$.

Such outcomes are further quantitatively verified by the computed integral errors in Tab. I which confirm the superior performance of the IMSA-MF-INLW over the IMSA-MF-CG. Furthermore, it is worth highlighting that the IMSA-MF-INLW exhibits a higher computational efficiency thanks to the faster technique exploited at each multi-zooming step to solve the MF subsurface inverse scattering problem (Tab. II).

Finally, it is also interesting to show the "evolution" of the reconstruction at different IMSA steps to point out the effectiveness of the synthetic zoom implemented through the external iterative process (outermost loop). For instance, the maps of both the real and the imaginary parts of the contrast function at each *s*-th ($s = 1, …, S$) step when illuminating the subsurface scenario with $V = 41$ probing sources are reported in Fig. 13. It is pictorially evident the non-negligible improvement of the data inversion iteration after iteration.

VI. CONCLUSION

A new method for the multi-frequency electromagnetic reconstruction of the dielectric properties of buried regions from GPR data has been presented. The proposed inversion algorithm is built on a three-loop structure. The external iterations perform a sequential adaptive refinement and shrinking of the region of interest where the target is assumed to be located. The dielectric properties of the regions of interest are then retrieved by means of a nonlinear inexact-Newton-based reconstruction approach, which is able to simultaneously process multi-frequency input data, whose innermost Landweber loop features L^p-space regularization capabilities.

As a first step of the validation process, the calibration parameters of the proposed inversion approach have been set by considering synthetic data to define the optimal working/inversion conditions. Then, the reconstruction performances of the proposed method have been preliminary assessed in a simulated environment with scattering data blurred with an additive noise. The key part of the method assessment has been the testing against experimental measurement in a real scenario. Towards this end, the reconstruction of a buried sandstone rock has been successfully carried out also in a comparative fashion. As a matter of fact, the behavior of the IMSA-MF-INLW method has been compared with that of a standard/single-resolution inexact-Newton technique as well as with another competitive multifrequency CG-based approach, with promising results.

REFERENCES

[1] L. B. Conyers, *Ground-penetrating Radar for Archaeology, 3rd Ed.* Lantham, Maryland, USA: Rowman& Littlefield, 2013.

[2] M. A. González-Huici, I. Catapano, and F. Soldovieri, "A comparative study of GPR reconstruction approaches for landmine detection," *IEEE J. Sel. Topics Appl. Earth Observ. Remote Sens.*, vol. 7, no. 12, pp. 4869-4878, Dec. 2014.

[3] D. Hu, S. Li, J. Chen and V. Kamat, "Detecting, locating, and characterizing voids in disaster rubble for search and rescue", *Adv. Eng. Inform.*, vol. 42, p. 100974, 2019.

[4] Lesselier and T. Habashy, Special issue on "Electromagnetic imaging and inversion on the Earth's subsurface," *Inverse Prob.*, vol. 16, no. 5, pp. 1083-1375, Oct. 2000.

[5] C.-C. Chen, J. T. Johnson, M. Sato, and A. G. Yarovoy, Special issue on "Subsurface sensing using ground-penetrating radar," *IEEE Trans. Geosci. Remote Sens.*, vol. 45, no. 8, pp. 2419-2421, Aug. 2007.

[6] D. J. Daniels, *Ground penetrating radar*, 2nd ed. London: Institution of Electrical Engineers, 2004.

[7] R. Persico, *Introduction to Ground Penetrating Radar: Inverse Scattering and Data Processing*. Hoboken, New Jersey: Wiley, 2014.

[8] S. Sun, B. J. Kooij and A. G. Yarovoy, "Linearized 3-D electromagnetic contrast source inversion and its applications to half-space configurations," *IEEE Trans. Geosci. Remote Sens.*, vol. 55, no. 6, pp. 3475-3487, Jun. 2017.

[9] A. Baussard, E. L. Miller, and D. Lesselier, "Adaptive multiscale reconstruction of buried objects," *Inverse Prob.*, vol. 20, pp. S1-S15, Dec. 2004.

[10] J. Wang, P. Aubry and A. Yarovoy, "Efficient implementation of GPR data inversion in case of spatially varying antenna polarizations," *IEEE Trans. Geosci. Remote Sens.*, vol. 56, no. 4, pp. 2387-2396, Apr. 2018.

[11] M. Salucci, G. Oliveri, and A. Massa, "GPR prospecting through an inverse-scattering frequency-hopping multifocusing approach," *IEEE*

Trans. Geosci. Remote Sens., vol. 53, no. 12, pp. 6573–6592, Dec. 2015, doi: 10.1109/TGRS.2015.2444391.

[12] M. Salucci, G. Oliveri, A. Randazzo, M. Pastorino, and A. Massa, "Electromagnetic subsurface prospecting by a fully nonlinear multifocusing inexact Newton method," *J. Opt. Soc. Am. A*, vol. 31, no. 12, p. 2618, Dec. 2014, doi: 10.1364/JOSAA.31.002618.

[13] M. Salucci *et al.*, "Three-dimensional electromagnetic imaging of dielectric targets by means of the multiscaling inexact-Newton method," *J. Opt. Soc. Am. A*, vol. 34, no. 7, pp. 1119–1131, Jul. 2017, doi: 10.1364/JOSAA.34.001119.

[14] S. Caorsi, M. Donelli, D. Franceschini, and A. Massa, "A new methodology based on an iterative multiscaling for microwave imaging," *IEEE Trans. Microw. Theory Tech.*, vol. 51, no. 4, pp. 1162–1173, Apr. 2003, doi: 10.1109/TMTT.2003.809677.

[15] M. Donelli, G. Franceschini, A. Martini, and A. Massa, "An integrated multiscaling strategy based on a particle swarm algorithm for inverse scattering problems," *IEEE Trans. Geosci. Remote Sens.*, vol. 44, no. 2, pp. 298–312, Feb. 2006, doi: 10.1109/TGRS.2005.861412.

[16] G. Bozza, C. Estatico, M. Pastorino, and A. Randazzo, "Application of an inexact-Newton method within the second-order Born approximation to buried objects," *IEEE Geosci. Remote Sens. Lett.*, vol. 4, no. 1, pp. 51–55, Jan. 2007, doi: 10.1109/LGRS.2006.885864.

[17] C. Estatico, M. Pastorino, and A. Randazzo, "A novel microwave imaging approach based on regularization in Lp Banach spaces," *IEEE Trans. Antennas Propag.*, vol. 60, no. 7, pp. 3373–3381, Jul. 2012, doi: 10.1109/TAP.2012.2196925.

[18] O. M. Bucci, L. Crocco, T. Isernia, and V. Pascazio, "Inverse scattering problems with multifrequency data: reconstruction capabilities and solution strategies," *IEEE Trans. Geosci. Remote Sens.*, vol. 38, no. 4, pp. 1749–1756, Jul. 2000, doi: 10.1109/36.851974.

[19] C. Estatico, A. Fedeli, M. Pastorino, and A. Randazzo, "A multifrequency inexact-Newton method in Lp Banach spaces for buried objects detection," *IEEE Trans. Antennas Propag.*, vol. 63, no. 9, pp. 4198–4204, Sep. 2015, doi: 10.1109/TAP.2015.2446995.

[20] C. Estatico, A. Fedeli, M. Pastorino, and A. Randazzo, "A Banach space regularization approach for multifrequency microwave imaging," *Int. J. Antennas Propag.*, vol. 2016, Art. ID 9304371, 2016, doi: 10.1155/2016/9304371.

[21] C. Estatico, A. Fedeli, M. Pastorino, and A. Randazzo, "Microwave imaging by means of Lebesgue-space inversion: An overview," *Electronics*, vol. 8, no. 9, p. 945, Sep. 2019, doi: 10.3390/electronics8090945.

[22] D. C. Stinson, *Intermediate mathematics of electromagnetics*. Englewood Cliffs, N.J.: Prentice-Hall, 1976.

[23] C. Estatico, A. Fedeli, M. Pastorino, and A. Randazzo, "Buried object detection by means of a LpBanach-space inversion procedure," *Radio Sci.*, vol. 50, no. 1, pp. 41–51, Jan. 2015, doi: 10.1002/2014RS005542.

[24] O. M. Bucci and G. Franceschetti, "On the degrees of freedom of scattered fields," *IEEE Trans. Antennas Propag.*, vol. 37, no. 7, pp. 918–926, Jul. 1989, doi: 10.1109/8.29386.

[25] O. M. Bucci and T. Isernia, "Electromagnetic inverse scattering: retrievable information and measurement strategies," *Radio Sci.*, vol. 32, no. 6, pp. 2123–2137, Nov. 1997, doi: 10.1029/97RS01826.

[26] O. M. Bucci, L. Crocco, T. Isernia, and V. Pascazio, "Subsurface inverse scattering problems: Quantifying, qualifying, and achieving the available information," *IEEE Trans. Geosci. Remote Sens.*, vol. 39, no. 11, pp. 2527–2538, Nov. 2001, doi: 10.1109/36.964991.

[27] A. Giannopoulos, "Modelling ground penetrating radar by GprMax," *Constr. Build. Mater.*, vol. 19, no. 10, pp. 755–762, Dec. 2005, doi: 10.1016/j.conbuildmat.2005.06.007.

[28] C. Warren, A. Giannopoulos, and I. Giannakis, "gprMax: Open source software to simulate electromagnetic wave propagation for Ground Penetrating Radar," *Comput. Phys. Commun.*, vol. 209, pp. 163–170, Dec. 2016, doi: 10.1016/j.cpc.2016.08.020.

[29] M. Salucci, L. Poli, and A. Massa, "Advanced multi-frequency GPR data processing for non-linear deterministic imaging," *Signal Process.*, vol. 132, pp. 306–318, Mar. 2017, doi: 10.1016/j.sigpro.2016.06.019.

[30] M. Salucci, L. Poli, N. Anselmi, and A. Massa, "Multifrequency particle swarm optimization for enhanced multiresolution GPR Microwave Imaging," *IEEE Trans. Geosci. Remote Sens.*, vol. 55, no. 3, pp. 1305–1317, Mar. 2017, doi: 10.1109/TGRS.2016.2622061.

[31] "Geophysics Test Sites – Near Surface Geophysics Group." http://www.nsgg.org.uk/2018/geophysics-test-sites/ (accessed Jul. 08, 2020).

[32] "NSGG UXO Test Site," *Geomatrix Earth Science Limited*. https://www.geomatrix.co.uk/tools/nsgg-uxo-test-site/ (accessed Jul. 07, 2020).

[33] A. Martinez and A. P. Byrnes, "Modeling dielectric constant values of geologic materials: an aid to ground-penetrating radar data collection and interpretation," *Curr. Res. Earth Sci.*, vol. Bulletin no. 247, Part 1, 2001.